PHYSICS OF FLUIDS **26**, 026601 (2014)

Anelastic internal wave reflection and transmission in uniform retrograde shear

Lauren Eberly[1] and Bruce R. Sutherland[1,2,a)]
[1]*Department of Earth and Atmospheric Sciences, University of Alberta, Edmonton, Alberta T6G 2E3, Canada*
[2]*Department of Physics, University of Alberta, Edmonton, Alberta T6G 2E1, Canada*

(Received 27 September 2013; accepted 22 January 2014; published online 7 February 2014)

We perform fully nonlinear simulations in two dimensions of a horizontally periodic, vertically localized, anelastic internal wavepacket in order to examine the effects of weak and strong nonlinearity upon wavepackets approaching a reflection level in uniform retrograde shear. Transmission, reflection, and momentum deposition are measured in terms of the horizontal momentum associated with the wave-induced mean flow. These are determined in part as they depend upon the initial wavenumber vector, $\vec{k} = (k, m)$, which determines the modulational stability (if $|m/k| \gtrsim 0.7$) or instability (if $|m/k| \lesssim 0.7$) of moderately large amplitude quasi-monochromatic internal wavepackets. Whether modulationally stable or unstable, the evolution of the wavepacket is determined by the height of the reflection level predicted by linear theory, z_r, relative to the height, z_Δ, at which weak nonlinearity becomes significant, and the height, $z_b > z_\Delta$, at which linear theory predicts anelastic waves first overturn in the absence of shear. If $z_r < z_\Delta$, the amplitude remains sufficiently small and the waves reflect as predicted by linear theory. If z_r is moderately larger than z_Δ, a fraction of the momentum associated with the wavepackets transmits past the reflection level. This is because the positive shear associated with the wave-induced mean flow can partially shield the wavepacket from the influence of the negative background shear enhancing its transmission. The effect is enhanced for weakly nonlinear modulational unstable wavepackets that narrow and grow in amplitude faster than the anelastic growth rate. However, as nonlinear effects become more pronounced, a significant fraction of the momentum associated with the wavepacket is irreversibly deposited to the background below the reflection level. This is particularly the case for modulationally unstable wavepackets, whose enhanced amplitude growth leads to overturning below the predicted breaking level. Because the growth in the amplitude envelope of modulationally stable wavepackets is retarded by weakly nonlinear effects, reflection is enhanced and transmission retarded relative to their modulationally unstable counterparts. Applications to mountain wave propagation through the stratosphere in the winter hemisphere are discussed. © *2014 AIP Publishing LLC*. [http://dx.doi.org/10.1063/1.4864104]

I. INTRODUCTION

Internal waves, driven by buoyancy forces, exist ubiquitously in the stratified atmosphere. When generated by wind forcing over topography, they propagate upward through the troposphere into the middle atmosphere. In doing so, these waves transport horizontal momentum vertically upward until being deposited at high altitudes where wave breaking occurs.[1]

Internal waves in the atmosphere have small length scales compared to the large-scale circulation. However, the momentum carried by the waves, and subsequent momentum deposition at high

a)Email: bruce.sutherland@ualberta.ca. URL: www.ualberta.ca/~bsuther.

altitudes where waves become unstable, has been found cumulatively and non-negligibly to affect mean zonal winds and corresponding temperatures associated with the general circulation.[2–4]

Being small scale, it is computationally prohibitive to resolve internal wave dynamics in general circulation models (GCMs).[5] As a method to include internal waves without resolving their dynamics, the momentum transport and drag associated with internal waves are parameterized in general circulation models. In part, these gravity wave drag parameterization schemes attempt to capture momentum deposition due to wave breaking at critical levels.[4,6,7] In a shear flow, this is where the horizontal phase speed of the waves matches the background flow speed or, equivalently, where the Doppler-shifted frequency of the waves is zero.[8,9] The breaking of internal gravity waves induces an energy cascade which creates disturbances at smaller and smaller scales.[10] Eventually the energetic scales become so small that they dissipate due to viscosity and thermal diffusion. Concurrently, the wave momentum flux divergence results in momentum that is deposited irreversibly to the background flow providing an acceleration in the direction of the phase speed relative to the background wind.[11]

Because the background density of the atmosphere decreases significantly with height, the amplitudes of waves grow as they propagate upward, thus providing another mechanism for wave breaking. The gravity wave drag parameterization scheme proposed by Lindzen[6] used linear anelastic theory to estimate where wave breaking occurs and, consequently, where momentum is deposited. This scheme has improved the accuracy of GCMs.[2–4] Wave breaking, however, is an inherently nonlinear process and so the accuracy of linear theory to predict momentum deposition due to anelastic growth and breaking is questionable.

Sutherland[12] developed a weakly nonlinear theory of Boussinesq internal waves which, through comparison with fully nonlinear simulations, was shown accurately to model the evolution of large-amplitude waves. The onset of nonlinear dynamics was shown to result from "self-acceleration," in which the wavepacket established a wave-induced mean flow which, in turn, altered the structure of the wavepacket.[13,14] Even without the presence of a background flow, the wave-induced mean flow (analogous to the Stokes drift for surface waves) acted to Doppler-shift the frequency of an internal wavepacket—a significant effect for sufficiently large-amplitude waves. In particular, it was observed that when the vertical wavenumber, m, was sufficiently small relative to the horizontal wavenumber, k (specifically $|m/k| < 2^{-1/2}$) the vertical structure of the wavepacket envelope narrowed and steepened through modulational instability. For wavepackets containing larger vertical wavenumber waves, the envelope broadened faster than predicted by linear dispersion through modulational stability.[12]

The Boussinesq study was followed by the development of weakly nonlinear theory for internal waves in a non-Boussinesq liquid[15] and in an anelastic gas.[16] Consistent with Boussinesq theory, anelastic waves were found to be either modulationally stable at high vertical wavenumbers or unstable at low vertical wavenumbers, with marginal stability occurring for waves propagating at the fastest vertical group velocity.[16]

The weakly nonlinear effects of modulational stability and instability were shown to change the height of overturning significantly when compared with linear theory predictions:[16] modulationally unstable wavepackets, which narrow and peak, overturned well below the breaking level predicted by linear theory; modulationally stable wavepackets, which broaden quickly, overturned well above the breaking level predicted by linear theory. In some cases, the difference of observed and linear-theory predicted breaking heights was tens of kilometers.

These studies were performed for waves with zero or uniform background wind. There are few studies of large-amplitude internal waves in non-uniform background flows. Sutherland[17] presented a fully nonlinear numerical study of the evolution of Boussinesq internal waves in a uniform shear flow with uniform stratification.[18] The shear flow was oriented with flow speed increasing with height, its direction oriented opposite to the horizontal phase speed of the incident wavepacket. For a rightward, upward-propagating wave, the negative shear was established so that, according to linear theory, at a certain height, wave reflection would occur due to Doppler-shifting by the background wind. Explicitly, this occurred where the Doppler-shifted wave frequency matched the background buoyancy frequency.[19]

Consistent with linear theory, small-amplitude waves propagated upward to the reflection level and then propagated downward. However, for moderately large-amplitude waves, significant

momentum was found to transmit across the reflection level. This was shown to result from the positive shear associated with the wave-induced mean flow canceling the negative background shear.

Being restricted to the Boussinesq approximation, the study by Sutherland[17] of moderately large-amplitude waves in retrograde, uniform shear did not allow for anelastic growth as in Dosser and Sutherland,[16] though the latter study did not include shear. As the next step in developing an understanding of momentum transport by atmospheric internal waves, in this study we synthesize Sutherland[17] and Dosser and Sutherland[16] to study the evolution and momentum transport by anelastic waves approaching a reflection level in retrograde shear.

Specifically, we assess the proportion of momentum associated with the incident wavepacket that transmits above, reflects from, or is deposited moderately below the reflection level. Of particular physical and theoretical interest is the evolution of incident nearly hydrostatic wavepackets. These are modulationally stable and so weakly nonlinear effects should retard the wavepacket growth suggesting substantial reflection according to linear theory. However, when approaching the reflection level the Doppler-shifted wavepacket becomes modulationally unstable, suggesting the possibility of enhanced transmission or overturning. We examine how this behavior changes as it depends upon the predicted height of the reflection level relative to the predicted height at which weakly nonlinear effects are expected become important.

Section II reviews the theoretical background for small-amplitude anelastic waves, wave propagation in shear and weakly nonlinear theory. Section III presents the numerical method used to solve the fully nonlinear anelastic equations. Section IV presents qualitative results of anelastic wave propagation in shear, and quantitative results for transmission, reflection, and momentum deposition are given in Sec. V. Conclusions including a discussion on the application of this work to momentum transport in the atmosphere are given in Sec. VI.

II. THEORY

For simplicity, we consider an isothermal atmosphere with temperature T_0. From the ideal gas law and hydrostatic balance, the background density, $\bar{\rho}$, and pressure, $\bar{p}$, decrease with height, z, exponentially as

$$\bar{\rho} = \rho_0 \exp(-z/H_\rho) \tag{1}$$

and

$$\bar{p} = p_0 \exp(-z/H_\rho), \tag{2}$$

where ρ_0 is the reference density, $p_0 = \rho_0 R_a T_0$ is the reference pressure, R_a is the gas constant for air, and H_ρ is the density scale height. In an isothermal atmosphere, the density scale height is

$$H_\rho = \frac{R_a T_0}{g}, \tag{3}$$

in which g is gravity. The background potential temperature is

$$\bar{\theta} = \theta_0 e^{z/H_\theta}, \tag{4}$$

where $\theta_0 = T_0$ is the potential temperature at $z = 0$, and

$$H_\theta = \kappa^{-1} H_\rho, \tag{5}$$

where $\kappa \simeq 2/7$ for a diatomic gas. The stratification of the atmosphere is represented by the squared buoyancy frequency,

$$N^2 \equiv \frac{g}{\bar{\theta}} \frac{d\bar{\theta}}{dz}. \tag{6}$$

In particular, in uniform stratification $N^2 = g/H_\theta$ is constant.

TABLE I. The polarization relations for anelastic waves in a uniformly stratified fluid in terms of the mass streamfunction, *psi*, defined so that $\vec{u} = \frac{1}{\bar{\rho}}\nabla \times (\psi\,\hat{y})$. The phase is represented by $\phi = kx + mz - \omega t$ and $K^2 = k^2 + m^2 + 1/(4H_\rho^2)$. Derivatives of the dispersion relation used in the Schrödinger equation are given for anelastic internal waves in a uniformly stratified fluid. The horizontal and vertical wavenumbers are k and m, respectively.

Field	Relation to $A_{\psi 0}$
$\psi = Re(\rho_0 A_{\psi 0} e^{\imath\phi} e^{-z/2H_\rho})$	$A_{\psi 0}$
$u = Re(A_{u0} e^{\imath\phi} e^{z/2H_\rho})$	$A_{u0} = \left(-\imath m + \frac{1}{2H_\rho}\right) A_{\psi 0}$
$w = Re(A_{w0} e^{\imath\phi} e^{z/2H_\rho})$	$A_{w0} = \imath k A_{\psi 0}$
$\zeta = Re(A_{\zeta 0} e^{\imath\phi} e^{z/2H_\rho})$	$A_{\zeta 0} = K^2 A_{\psi 0}$
$\xi = Re(A_{\xi 0} e^{\imath\phi} e^{z/2H_\rho})$	$A_{\xi 0} = -\frac{K}{N} A_{\psi 0}$
$\theta = Re(A_{\theta 0} e^{\imath\phi} e^{z/2H_\rho})$	$A_{\theta 0} = \bar{\theta}' \frac{K}{N} A_{\psi 0}$
$\rho = Re(A_{\rho 0} e^{\imath\phi} e^{-z/2H_\rho})$	$A_{\rho 0} = -\frac{\rho_0}{H_\theta} \frac{K}{N} A_{\psi 0}$
Dispersion relation and m-derivatives	
$\omega = Nk/K$	
$c_{gz} = \omega_m = -Nkm/K^3$	
$\omega_{mm} = -N(3m^2 - K^2)k/K^5$	

In zero background flow, small-amplitude, two-dimensional anelastic plane waves of horizontal and vertical wavenumber k and m, respectively, satisfy the dispersion relation[19]

$$\omega^2 = N^2 \frac{k^2}{k^2 + m^2 + \frac{1}{4H_\rho^2}}. \tag{7}$$

This shows that anelastic internal waves are propagating only if the intrinsic frequency, ω, is less than N. The vertical group speed, $c_{gz} = \partial\omega/\partial m$, polarization relations, and other properties of small-amplitude anelastic internal waves are summarized in Table I.

Our study focuses upon the evolution of horizontally periodic, vertically localized, quasi-monochromatic wavepackets whose vertical structure is given in terms of an amplitude envelope, $A(z, t)$. For example, the vertical displacement field is

$$\xi = A_\xi(z, t) e^{i(kx+mz-\omega t)} e^{z/2H_\rho}, \tag{8}$$

where the second exponential captures the anelastic growth predicted by linear theory and it is understood that the actual displacement is the real part of the right-hand side of (8). The horizontal and vertical velocity fields, u and w, respectively, likewise exhibit exponential growth as $\exp(z/2H_\rho)$. Because the horizontally averaged vertical flux of horizontal momentum is defined by

$$F_M = \bar{\rho}\langle u w\rangle, \tag{9}$$

in which the angle brackets denote horizontal averaging, we see that F_M does not grow exponentially.

Because the waves are horizontally periodic, one can attribute horizontal momentum to the waves (an exception to the "wave momentum myth" paradigm[20]). Their momentum is $\bar{\rho}U$ in which U is the wave-induced mean flow, given explicitly by[14,19,21]

$$U(z, t) \equiv -\langle \xi\,\zeta\rangle, \tag{10}$$

in which ζ is the spanwise vorticity. Using the polarization relations in Table I, it can be shown that

$$U = \frac{1}{2} N K |A_\xi|^2 e^{z/H_\rho}, \tag{11}$$

in which $K^2 = k^2 + m^2 + 1/\left(4H_\rho^2\right)$. It can also be shown that the momentum flux is related to the momentum by

$$F_M = c_{gz}\,(\bar{\rho}U)\,, \tag{12}$$

which is analogous to the relationship between energy flux and energy. (This analogy is explained in detail in Fig. 3.7 and associated text of Sutherland.[19])

Waves overturn where the total potential temperature gradient is negative:

$$\frac{d\bar{\theta}}{dz} + \frac{\partial \theta}{\partial z} < 0, \tag{13}$$

in which θ is the fluctuation potential temperature. For plane, anelastic waves with vertical displacement amplitude $A_{\xi 0}$ at $z = 0$, (13) gives the linear theory prediction for the breaking height:[16]

$$z_b = 2H_\rho \ln\left(\frac{1}{|m A_{\xi 0}|}\right). \tag{14}$$

This prediction assumes that there is no background shear.

As a small-amplitude wavepacket moves vertically through a background wind, the extrinsic (Doppler-shifted) frequency, Ω, changes according to

$$\Omega = \omega - \bar{U}k. \tag{15}$$

In particular, if $\bar{U}$ decreases with height, the extrinsic frequency increases. Waves reflect where the extrinsic frequency of a wavepacket matches the background buoyancy frequency, N. In the specific case of linearly decreasing background horizontal velocity $\bar{U} = -s_0 z$, in which $-s_0 < 0$ is the constant background shear, linear theory predicts that the reflection height is situated at

$$z_r = \frac{N - \omega}{k s_0}. \tag{16}$$

Unlike the background flow, $\bar{U}$, the wave-induced mean flow, U, evolves transiently as the wavepacket evolves. Although the Stokes-drift of surface waves is relatively small even for waves near breaking amplitudes, the wave-induced mean flow of the internal waves can be substantial.[14] For example, using (14) in (11), the value of U at the breaking height is $(1/2)NK/m^2$. This can exceed the horizontal phase speed of the waves, N/K, and certainly does so for non-hydrostatic waves with $m \approx 0$, which is the case for waves near the reflection height. In reality, below the breaking height U acts weakly nonlinearly through Doppler-shifting the waves, which in turn changes the structure of U.

These nonlinear feedback effects are well-modeled by the nonlinear Schrödinger equation (NLS) that describes the evolution of the amplitude envelope of anelastic internal gravity waves in zero background wind:[16]

$$A_t + c_{gz} A_z = \imath \frac{1}{2} \omega_{mm} A_{zz} - \imath k U A, \tag{17}$$

in which U is given by (11) and, for writing convenience, we have defined $A \equiv A_\xi$ to be the amplitude envelope of the vertical displacement field, as in (8). The first term on the right-hand side of (17) denotes linear dispersion and the second (nonlinear) term denotes Doppler-shifting by the wave-induced mean flow, given by (11), which is strictly positive and proportional to $|A|^2$.

In general, the modulational stability or instability of a wavepacket is assessed by the relative signs of the coefficients of the dispersion and nonlinear terms.[22] Marginal stability occurs if $\omega_{mm} = 0$, corresponding to waves moving with the fastest vertical group velocity. This occurs for vertical wavenumber m_c such that

$$|m_c/k| = 2^{-1/2}\left[1 + \frac{1}{(2kH_\rho)^2}\right]^{1/2}. \tag{18}$$

In the special case of $kH_\rho \gg 1$, the relative vertical wavenumber of marginally stable anelastic waves is identical to that for Boussinesq waves:[12] $|m_c/k| = 1/\sqrt{2}$.

If $m < m_c < 0$ then $\omega_{mm} > 0$ and the wavepacket is modulationally stable. Hence, the wavepacket widens at a rate faster than that due to linear dispersion and anelastic growth of the amplitude is reduced. This is because the wave-induced mean flow Doppler-shifts the waves to larger vertical

wavenumbers which move with faster vertical group speed, causing the wavepacket to spread out. For $m_c < m < 0$, $\omega_{mm} < 0$ and the wavepacket is modulationally unstable; the Doppler-shifted waves move with slower vertical group speed causing the wavepacket to narrow and steepen.

Dosser and Sutherland[16] estimated the height, z_Δ, at which the weakly nonlinear effects become sufficiently large for the effects of modulational stability or instability to become non-negligible:

$$z_\Delta = 2H_\rho \ln\left(\frac{1}{A_{\xi 0}K^2}\sqrt{\frac{2\Delta|m|}{\sigma}}\right), \tag{19}$$

where $\Delta \approx 1$ represents the magnitude of the ratio of the leading nonlinear term to the advection term in (17), and σ is the vertical extent of the wavepacket. In uniform flow, modulationally unstable waves were found to overturn between z_Δ and z_b due to the accentuated amplitude growth. Modulationally stable waves were found to propagate well above z_b because their anelastic growth rate was reduced by the enhanced spreading of the wavepacket. In fact, for larger $|m/k|$, waves were able to propagate many density scale heights above the breaking height predicted by linear theory.[16]

Sutherland[17] found that when Boussinesq waves approached a reflection level, their amplitude doubled as the incident, upward-propagating waves combined with the reflected, downward-propagating waves. This in turn quadrupled the wave-induced mean flow which caused sufficiently large amplitude waves to be Doppler-shifted to higher frequencies and, thus, begin to reflect at heights below z_r. However, as the trailing edge of the wavepacket approached the reflection level, the amplitude of the incident and reflected waves decreased causing a shift to lower frequency and thus a portion of the wavepacket transmitted through the reflection level. These transmitted waves eventually either reflected or dissipated at high levels due to continual Doppler-shifting by the background wind. That study provided criteria for when significant transmission would occur. But it did not assess relative transmission and reflection of momentum above and below z_r.

III. METHODS

The equations used in the code were non-dimensionalized by using the time scale, N^{-1}. For all cases, N remained fixed. Likewise, the length scale, k^{-1}, was fixed in all simulations. In what follows, the equations and analyses are given in units of k and N. All simulations were done using a fully nonlinear, 2D, anelastic code that implicitly solved for spanwise vorticity, ζ, and potential temperature, θ. For now excluding viscosity and diffusion, the vorticity equation is[16]

$$\frac{D\zeta}{Dt} = -\frac{1}{H_\rho}w\zeta - \frac{g}{\bar{\theta}}\frac{\partial\theta}{\partial x}, \tag{20}$$

and the internal energy equation is

$$\frac{D\theta}{Dt} = -w\frac{d\bar{\theta}}{dz}. \tag{21}$$

Particularly to avoid the exponential growth of small-scale disturbances near the top of the domain, the code solved the equations of motion written in terms of variables that filtered out the anelastic growth predicted by linear theory. For example, the anelastic-filtered ("hatted") variables representing spanwise vorticity, vertical displacement, and horizontal and vertical velocities are given implicitly by $(\zeta, \xi, u, w) = (\hat{\zeta}, \hat{\xi}, \hat{u}, \hat{w})e^{z/2H_\rho}$. The details of the transformation of (20) and (21) to anelastic-filtered variables are provided in the Appendix.

Thus, with the inclusion of diffusion terms, (20) and (21) are

$$\frac{\partial}{\partial t}\hat{\zeta} = -\bar{U}\hat{\zeta}_x + e^{z/2H_\rho}\left[-\hat{u}\hat{\zeta}_x - \hat{w}\hat{\zeta}_z - \frac{3}{2H_\rho}\hat{w}\hat{\zeta}\right] + N^2\hat{\xi}_x + C_\zeta\nabla^2\hat{\zeta}, \tag{22}$$

$$\frac{\partial}{\partial t}\hat{\xi} = -\bar{U}\hat{\xi}_x + e^{z/2H_\rho}\left[-\hat{u}\hat{\xi}_x - \hat{w}\hat{\xi}_z - \left(\frac{1}{2H_\rho} + \frac{1}{H_\theta}\right)\hat{w}\hat{\xi}\right] + \hat{w} + C_\theta\nabla^2\hat{\xi}, \tag{23}$$

in which the advective terms of the material derivative, including the background mean flow, have been put on the right-hand side of the equations. Also, (21) has been recast in terms of the approximate vertical displacement using $\xi \equiv -\theta/(d\bar{\theta}/dz)$. The anelastic-filtered streamfunction, $\hat{\psi}$, is implicitly related to vorticity using (A3) and (A10) to give

$$\hat{\zeta} = -\nabla^2\hat{\psi} + \frac{1}{4H_\rho^2}\hat{\psi}. \tag{24}$$

This is inverted to find $\hat{\psi}$ for given $\hat{\zeta}$. The anelastic-filtered velocities are found from (A1) and (A2):

$$\hat{u} = -\frac{\partial\hat{\psi}}{\partial z} + \frac{1}{2H_\rho}\hat{\psi}, \tag{25}$$

$$\hat{w} = \frac{\partial\hat{\psi}}{\partial x}. \tag{26}$$

In order to ensure numerical stability, but not at the expense of excessive wave damping, the coefficients C_ζ and C_θ of the dissipation terms $C_\zeta\nabla^2\hat{\zeta}$ and $C_\theta\nabla^2\hat{\xi}$ were chosen to be zero throughout the domain for waves with horizontal wavenumber $k < 17$. For larger horizontal wavenumbers, $C_\zeta = C_\theta = 10^{-4}N/k^2$ throughout most of the domain. Hence, small-scale noise was sufficiently damped throughout wave propagation and breaking. To inhibit downward propagating disturbances from the top of the domain, C_ζ and C_θ were enhanced over the top 20% of the domain. This also acted as a sponge layer to damp out noise that tended to grow more rapidly where the background density was small. From the bottom of the sponge layer to the upper bound of the domain, viscosity linearly increased a hundredfold from its background viscosity. Equations (22) and (23) were solved using a mixed spectral, finite-difference scheme. The code advanced in time by a leap-frog method with Euler back-steps performed every 20 time steps.[23]

The vertical extent of the domain ranged from $z = -30k^{-1}$ to between $120k^{-1}$ and $300k^{-1}$ with larger values chosen in simulations with greater expected height of wave reflection. This ensured that the wavepacket remained far from both boundaries during its evolution. Free-slip boundary conditions were used on both the top and bottom of the domain. The domain was resolved with a vertical grid spacing of $\Delta z = 0.02k^{-1}$. Horizontally, the domain was periodic and set to resolve wavenumbers up to $16k$. Doubling the vertical spatial and horizontal wavenumber resolution had no significant effect on the observed wave dynamics.

The code was initialized with constant background stratification, exponentially decreasing background density $\bar{\rho} = \rho e^{-z/H_\rho}$, and uniform background shear $\bar{U} = U_0 - s_0 z$ with U_0 and s_0 constant, as described below. Additionally, simulations were conducted with a range of background density scale heights ranging from $H_\rho = 10k^{-1}$ to $30k^{-1}$. Most simulations examined the case with $kH_\rho = 20$, corresponding to mesoscale atmospheric internal waves with a horizontal wavelength of approximately 2.5 km.

Superimposed on this background was an anelastic, horizontally periodic, vertically Gaussian, quasi-monochromatic wavepacket centered at $z = 0$. The amplitude envelope was initialized according to

$$\hat{\xi}(x, z, 0) = \frac{1}{2}A_0 \exp\left(-z^2/2\sigma^2\right) e^{i(kx+mz)} + c.c., \tag{27}$$

in which $c.c.$ denotes the complex conjugate. The vertical extent of the wavepacket was $\sigma = 10k^{-1}$ which ensured the wavepacket was quasi-monochromatic. The initial wavepacket was set to have amplitude $A_0 = 0.05k^{-1}$, which was small enough that the polarization relations of linear theory could be applied to initialize the other fields and was large enough that weakly nonlinear effects were expected to develop shortly after the wavepacket began to move upward and grow anelastically. Making use of the polarization relations (Table I), the initial anelastic-filtered vorticity was given as in (27) but with A_0 replaced by $-NKA_0$. Even at the initial time step, there was some flow induced by the waves themselves, $U = -\langle\xi\zeta\rangle$. However, it was small. The background flow at $z = 0$ was set to be $U_0 = -c_{px}$ where $c_{px} = \omega/k$ represents the initial intrinsic horizontal phase speed of the

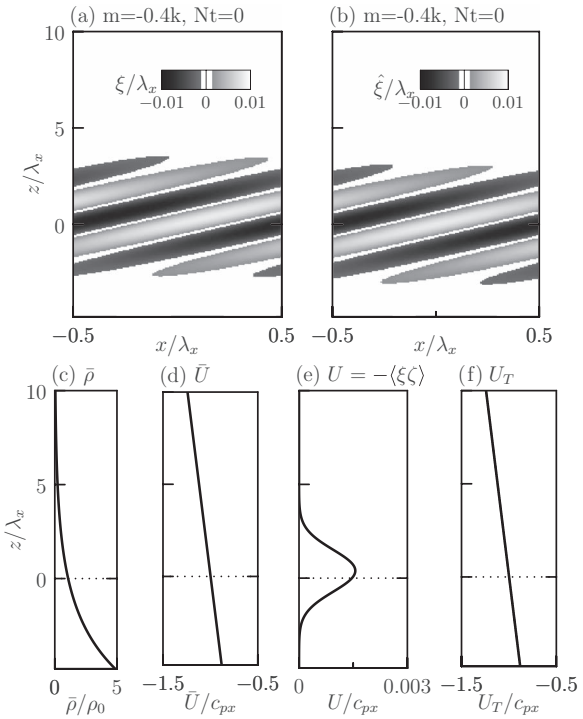

FIG. 1. Both (a) and (b) show a snapshot of anelastic waves for $m = -0.4k$, $z_r = H_\rho$ waves at $Nt = 0$. The displacement field, ξ, is given in (a) and the density-scaled displacement field, $\hat{\xi}$, is shown in (b). (c) An example background density profile, $\bar{\rho}$, and (d) a background velocity profile, $\bar{U}$. The wave-induced mean flow is shown in (e) and the superposition of (d) and (e), giving U_T, is shown in (f).

waves. This ensured that while the waves had small amplitude, their horizontal phase did not change in time, which helped to visualize Doppler-shifting effects particularly when examining movies of the simulations.

An example of the initial state is shown in Figure 1. The displacement field, ξ, is shown in Fig. 1(a). Although these waves are vertically confined to less than one density scale height, it is evident that the anelastic-filtered $\hat{\xi}$ field in Fig. 1(b) has smaller amplitude at the leading edge of the wavepacket due to the smaller background density. Likewise, $\hat{\xi}$ is larger than ξ at the trailing edge. This difference between ξ and $\hat{\xi}$ became more obvious when waves propagated upward over many density scale heights such that $\|\xi\|$ grew exponentially and $\|\hat{\xi}\|$ remained constant until weakly nonlinear effects became important.

Figure 1(c) shows a typical background density profile and Fig. 1(d) shows the background wind for a case where reflection occurs at $z_r = H_\rho$. Figure 1(e) shows the initial wave-induced mean flow, $U = -\langle\xi\zeta\rangle$. The total flow, $U_T = \bar{U} + U$, is the superposition of the wave-induced mean flow and the background shear, as shown in Figure 1(f). The addition of U to $\bar{U}$ is barely distinguishable from $\bar{U}$ alone (see Figure 1(d)), consistent with the condition that the initial wavepacket had small-amplitude.

In an effort to investigate the behavior of modulationally stable, marginally stable, and modulationally unstable waves, our simulations focused primarily upon a range of wavepackets that had initial wavenumbers of $m = -1.4k$, $-0.7k$, and $-0.4k$, respectively. Waves were allowed to propagate to various reflection heights ranging from $z_r = H_\rho$ to $z_r = 8H_\rho$, as set by the value of the background shear through (16). The initial vertical extent of the wavepacket was also varied to ensure that the wavepacket was initially quasi-monochromatic. In most cases $\sigma = 10k^{-1}$, but we also set $\sigma = 3k^{-1}$ in large $|m/k|$ simulations.

The simulation run time was estimated from the reflection height and the vertical group speed, c_{gz}. The time for the wavepacket to reach the reflection level was roughly estimated using $t_r = z_r/c_{gz}$ and simulations were run up to time $4t_r$. Time steps of $\Delta t = 0.005N^{-1}$ were used.

The profile of horizontal momentum associated with the waves was calculated by multiplying the difference of the total and background horizontal mean flow by the background density. We denote the result by $\bar{\rho}\langle u\rangle \equiv \bar{\rho}(U_T - \bar{U})$. Consistent with Dosser and Sutherland,[16] we confirmed that $\langle u\rangle = U\,(=-\langle \xi\zeta\rangle)$ for all z and t up to the point of wave dissipation. When the waves grew so large that they dissipated, the associated momentum became irreversibly deposited to the background.

Whether or not the waves dissipated, the total momentum

$$M_T = \int_{z_{min}}^{z_{max}} \bar{\rho}\langle u\rangle dz \tag{28}$$

was conserved.

This fact was used to measure the transmission, reflection, and deposition of momentum by waves in retrograde shear. We define the vertically integrated momentum in the upper, middle, and lower parts of the domain by

$$M_U = \int_{z_r}^{z_{max}} \bar{\rho}\langle u\rangle dz, \tag{29}$$

$$M_M = \int_{H_\rho}^{z_r} \bar{\rho}\langle u\rangle dz, \tag{30}$$

and

$$M_L = \int_{z_{min}}^{H_\rho} \bar{\rho}\langle u\rangle dz, \tag{31}$$

respectively.

Here, the lower bound of the upper region is z_r (the linear-theory predicted reflection height) and the upper bound of the lower region is H_ρ, one density scale height above $z = 0$. The upper bound of the lower region was chosen to ensure that nearly all the momentum associated with the initial wavepacket was contained in the lower region at initial times and that the waves were able to propagate back into this region at late times. The transmission, reflection, and dissipation of waves were assessed by evaluating M_T, M_U, M_M, and M_L at late times in simulations when they were found to be near steady state. It was found that $t_{max} = 4t_r$ was a good assumption for the attainment of steady state as measurements of transmission and reflection became constant after $t \simeq 2.5t_r$. These late-time integrated total, upper-region, and lower-region momenta are denoted by M_T^∞, M_U^∞, and M_L^∞, respectively. The transmission of waves across the reflection level is thus defined in terms of the transmission coefficient

$$T \equiv \frac{M_U^\infty}{M_T^\infty}. \tag{32}$$

Similarly, the reflection coefficient is defined to be

$$R \equiv \frac{M_L^\infty}{M_T^\infty}. \tag{33}$$

The relative deposition of momentum below the reflection level (between the upper and lower regions) is given by

$$1 - (T + R). \tag{34}$$

IV. QUALITATIVE RESULTS

As a test of the code, simulations are run for the case where waves are predicted to reflect at $z_r = H_\rho$. Because the waves propagated only one density scale height before reaching the reflection

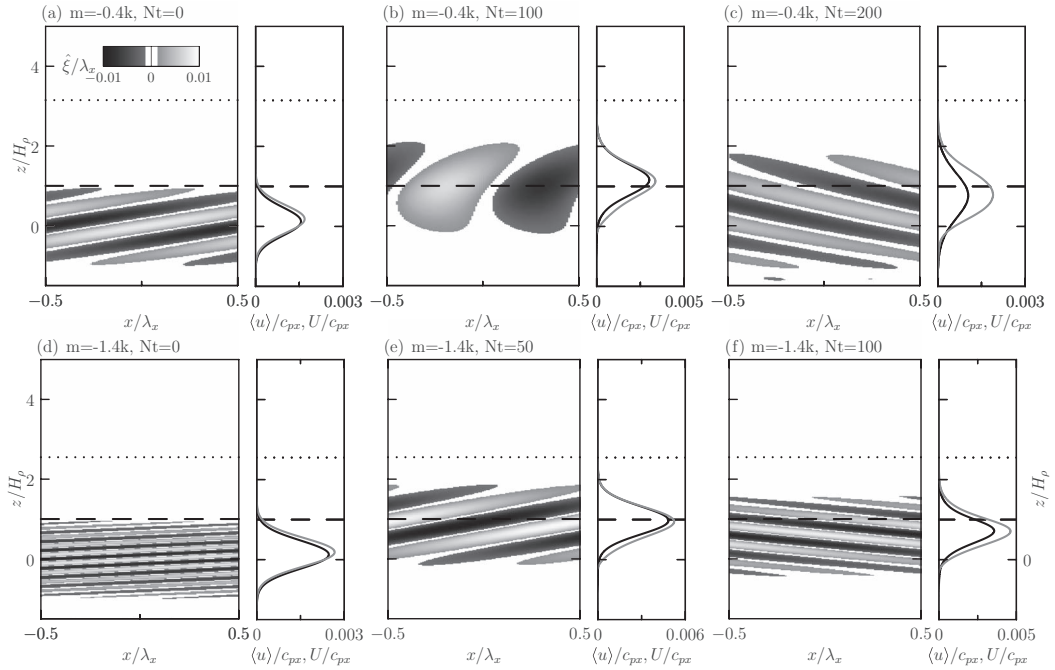

FIG. 2. Wavepacket evolution in simulations with $z_r = H_\rho$ and $kH_\rho = 20$ for ((a)–(c)) $m = -0.4k$ and ((d)–(e)) $m = -1.4k$. Results are shown for three times in each case, as indicated. Each plot shows (left) the anelastic-filtered vertical displacement field normalized by horizontal wavelength, $\hat{\xi}/\lambda_x$ (grayscale) and plots (right) of the wave-induced mean flow, U (black line) compared with the horizontally averaged flow, $\langle u\rangle$ (gray line). The dashed lines indicate the predicted reflection height, z_r, and the dotted lines indicate the height, z_Δ, at which weakly nonlinear effects are expected to become important. Explicitly, $z_\Delta = 3.2H_\rho$ for $m = -0.4k$ and $z_\Delta = 2.6H_\rho$ for $m = -1.4k$. The corresponding overturning heights in the absence of shear as predicted by linear theory are (not shown) $z_b = 8.0H_\rho$ and $5.5H_\rho$.

level, their amplitude is expected to remain sufficiently small that they should evolve according to linear theory.

The results of simulations with $m = -0.4k$ and $m = -1.4k$ are shown in Figures 2(a)–2(c) and 2(d)–2(f), respectively. In both cases, $H_\rho = 20k^{-1}$. The initial states for the simulation results in Figures 2(a)–2(c) are shown in Figure 1.

In both cases, z_r (indicated by the dashed line) is below the height, z_Δ, given by (19), at which weakly nonlinear effects are expected to become significant (dotted line). Because $z_\Delta > z_r$ in both simulations the wavepacket evolution is well-predicted by linear theory. In the case $m = -0.4k$, as the waves approach the reflection level, the phase lines of the vertical displacement field tilt upward (Figure 2(b)), and then tilt downward to the right after reflection (Figure 2(c)). The wave-induced mean flow, U, and the difference of the horizontally averaged flow and the background, $\langle u\rangle \equiv U_T - \bar{U}$, is shown to the right of each displacement field plot. In all cases, U and $\langle u\rangle$ are small compared to c_{px}, indicating that there is insignificant Doppler-shifting of the waves by the wave-induced mean flow. That both curves are close to overlapping initially is consistent with the assertion that $\langle u\rangle$ is well represented by the correlations $U \equiv -\langle \xi\zeta\rangle$. Upon reflection, the profile of $\langle u\rangle$ lies moderately above the profile of U because the wavefield is composed of a superposition of the upward and downward waves. When the waves propagate well below the reflection level (not shown) the curves come close to overlapping once more. Thus negligible momentum is irreversibly lost to the background flow. The discrepancy between the wave-induced mean flow and the horizontally averaged background flow at late times is due to viscosity which, though small, still dissipated the waves to small degree.

If the reflection level is situated above the height at which weakly nonlinear effects become important, the evolution of the wavepackets is qualitatively different. This is illustrated in Figure 3, which shows the counterpart of the simulations in Figure 2 but with $z_r = 4H_\rho$. In both

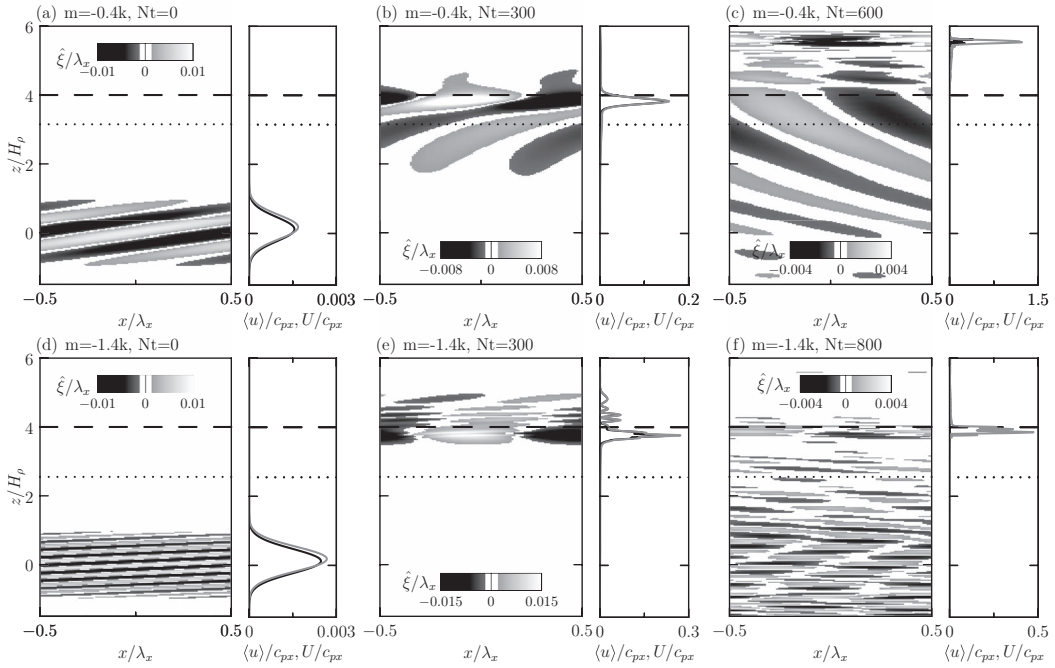

FIG. 3. ((a)–(f)) As in Fig. 2 but for simulations in which the background shear is weaker such that $z_r = 4H_\rho$. The values of z_Δ and z_b are the same as those given in the caption of Fig. 2.

simulations, the reflection level is located above z_Δ but is below the overturning level z_b. Explicitly, in Figs. 3(a)–3(c) for which $m = -0.4k$, $z_\Delta = 3.2H_\rho < z_r = 4H_\rho < z_b = 8.0H_\rho$ and in Figs. 3(d)–3(f) for which $m = -1.4k$, $z_\Delta = 2.6H_\rho < z_r = 4H_\rho < z_b = 5.3H_\rho$.

As the wavepacket with $m = -0.4k$ approaches the reflection level (Figure 3(b)), the phase lines tilt somewhat toward the vertical but, because the wavepacket is modulationally unstable, the wavepacket narrows and grows in amplitude. The magnitude of the wave-induced mean flow grows substantially, increasing to $0.16\,c_{px} \simeq 0.15\,N/k$ over a distance of H_ρ. From (16), the background shear in this case is $-s_0 = -(N - \omega)/(4kH_\rho) \simeq -0.018N/(kH_\rho)$, which is smaller in magnitude than the characteristic shear, $||dU/dz||$, associated with the wave-induced mean flow. Thus the wave-induced mean flow partially shields the wavepacket from the influence of the background shear, permitting it to propagate above the reflection level. This becomes clear by time $Nt = 600$ (Figure 3(c)) when a relatively small portion of the wavepacket has reflected but the rest has transmitted across the reflection level. At this time the horizontally averaged flow, $\langle u\rangle$, peaks well above the reflection level with values comparable to c_{px}. U is small compared to $\langle u\rangle$ at this time indicating that the difference in the mean horizontal flow from the background is due to irreversible deposition of momentum from the wave to the background.

The corresponding simulation for a modulationally stable wavepacket is shown in Figures 3(d)–3(f). Even though the amplitude envelopes of modulationally stable wavepackets spread and do not grow as fast as predicted by linear anelastic theory, only a small portion of the wavepacket reflects and undergoes downward propagation. Instead, the shear associated with the wave-induced mean flow peaks just below the reflection level (Figure 3(e)) with a small portion of the wavepacket transmitting and continuing upward propagation. The wave-induced mean flow below z_r at this time peaks at $0.49\,c_{px} \simeq 0.28/\,N/k$, changing over half a density scale height. The shear associated with this is approximately equal to the background shear of magnitude $s_0 \simeq 0.10N/(kH_\rho)$, but not so large that the wavepacket is shielded from the effects of the background flow as in Figs. 3(a)–3(c). Unlike the previous case, the wavepacket does not peak and continue upward propagation. Long after reflection (Figure 3(f)) the majority of the momentum associated with the wavepacket is irreversibly deposited to the background with an increase to the background mean

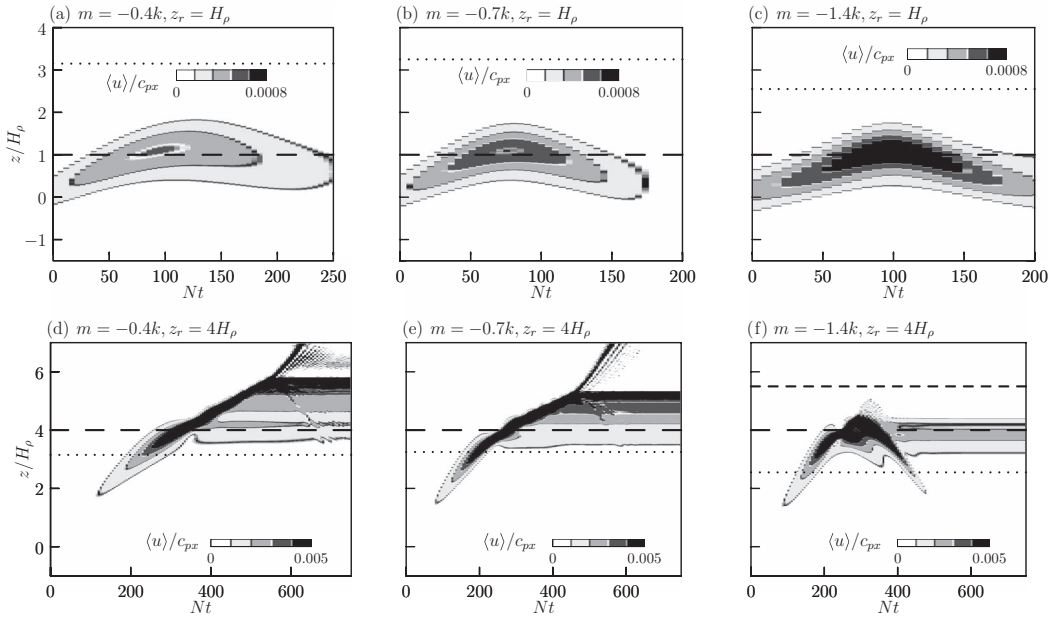

FIG. 4. Time series of vertical profiles of the normalized mean flow, $\langle u\rangle/c_{px}$, from simulations with $z_r = H_\rho$ and (a) $m = -0.4k$, (b) $m = -0.7k$, and (c) $m = -1.4k$ and with $z_r = 4H_\rho$ and (d) $m = -0.4k$, (e) $m = -0.7k$, and (f) $m = -1.4k$. In all cases $kH_\rho = 20$. Dashed and dotted lines represent the heights, z_r and z_Δ, respectively. The linear theory predicted breaking heights (in the absence of nonuniform shear) are ((a) and (d)) $z_b = 8.0H_\rho$, ((b) and (e)) $z_b = 7.0H_\rho$, and ((c) and (f)) $z_b = 5.5H_\rho$. The breaking level is shown in (f) as the short-dashed line.

flow just below the reflection level due to the leading portion of the reflected wavepacket combining with the upward-propagating trailing portion.

The transport and deposition of momentum is clearly illustrated by vertical time series $\langle u\rangle$, as shown in Figure 4. Figures 4(a)–4(c) show three simulations for the case in which $z_r = H_\rho < z_\Delta$ so that weakly nonlinear effects remain insignificant. In particular, the time series in Figures 4(a) and 4(c) correspond to the simulations shown in Figures 2(a)–2(c) and 2(d)–2(f), respectively. Figures 4(d)–4(f) show corresponding time series from simulations with $z_r = 4H_\rho > z_\Delta$, with Figures 4(d) and 4(f) corresponding to the simulations shown in Figures 3(a)–3(c) and 3(d)–3(f), respectively. Figures 4(b) and 4(e) show the results from simulations of a marginally stable wavepacket with $m = -0.7k$ and $z_r = H_\rho$ and $4H_\rho$, respectively.

In the simulations with $z = H_\rho$, for which the waves remain small amplitude while reflecting, the mean flow grows as the wavepacket approaches z_r and then returns approximately to its initial value after reflecting and returning to its initial height. Some asymmetry in the mean flow associated with the upward- and downward-propagating wavepacket is observed in the case with $m = -0.4k$ as a result of linear dispersion (Fig. 4(a)): because the vertical extent of the incident wavepacket is $\sigma = 10k^{-1} = 4|m|^{-1}$ the wavepacket is more broad-banded, as compared to simulations with $|m| = 0.7k$ and $1.4k$.

In the three simulations with $z_r = 4H_\rho$, momentum is deposited to the background resulting in irreversible acceleration of the mean flow in each case. In the modulationally unstable case with $m = -0.4k$ (Figure 4(d)), momentum deposition occurs shortly after the wavepacket crosses the reflection level, though still well below the predicted breaking level (at $z_b = 8.0H_\rho$). The acceleration of the background increases as the wavepacket continues to propagate upward into the lower-density background until most of its associated momentum has dissipated. The maximum increase in flow speed occurs near $z = 5.5H_\rho$.

These results differ from those for simulations with $m = -0.4k$ in the Boussinesq study of Sutherland,[17] in which large-amplitude wavepackets deposited their momentum near but below z_r. Here, because the waves grow anelastically, the increasing amplitude of the disturbance above the

reflection level allows for the continual deposition of momentum with consequent increasing mean flow speeds with height.

In the marginally stable case with $m = -0.7k$ (Fig. 4(e)), the evolution of the mean flow is similar to the modulationally unstable case except the height of the maximum mean flow deposition occurs at a moderately lower height, $z \simeq 5H_\rho$. This is to be expected because, as the wavepacket approaches the reflection level, the waves are Doppler-shifted to lower vertical wavenumbers and so become modulationally unstable.

In the modulationally stable case with $m = -1.4k$, both momentum deposition and reflection are evident after propagating above z_Δ and reflecting at z_r, as shown in Figure 4(f). In this case, some background flow acceleration occurs near the reflection level but below the predicted breaking height of $z_b = 5H_\rho$. Even though this wavepacket is modulationally stable, as the wavepacket reflects, the leading edge of the wavepacket is superimposed upon the upward-propagating trailing edge and thus amplitude is doubled at this location. Nonlinear effects are enhanced at the reflection level which drives the wavepacket to breaking amplitudes.

V. QUANTITATIVE RESULTS

We crudely characterize the location of momentum deposition in simulations run with wide-ranging parameters by considering the vertically integrated momentum measurements in three domain regions according to (28), (29), and (31). Figure 5 shows how these change in time during a simulation in which $H_\rho = 20k$, $m = -1.4k$ and (a) $z_r = 2H_\rho$ and (b) $z_r = 4H_\rho$.

As expected from momentum conservation, M_T (dotted line) remains constant for the duration of the simulations. In both cases, the vertically integrated momentum in the lower domain, M_L (dashed line), is initially equal to M_T because the entire wavepacket is in this region. As time progresses and the wavepacket propagates upward toward the reflection level, momentum leaves the lower domain and M_L decreases while the momentum M_M in the middle region increases.

For the simulation results in Figure 5(a), the wavepacket reaches the reflection level around $Nt = 100$. At this time, a portion of the wavepacket extends evanescently across the reflection level resulting in an increase of the vertically integrated momentum in the upper region, M_U (solid line). During reflection, M_U and M_L do not sum to M_T. The difference is associated with the momentum between the upper and lower regions ($H_\rho \le z \le z_r$). After reflection the wavepacket propagates downward into the lower region once more as evident by the increase in M_L and decrease in M_U. After $Nt = 300$, the vertically integrated momenta in each domain have reached steady state with $M_T = M_T^\infty$, $M_L = M_L^\infty$, and $M_U = M_U^\infty$ for the remainder of the simulation. Even after propagating over only two density scale heights, the waves grow sufficiently in amplitude that weakly nonlinear effects became important. The wavepacket mostly reflects (similar to the fully linear simulation with $z_r = H_\rho$, Figure 2(c)). However, at late times some momentum is permanently deposited above the reflection level as indicated by the non-zero value of $M_U^\infty = 0.78M_T^\infty$. Furthermore, $M_U^\infty + M_L^\infty = 0.84M_T^\infty$ is less than M_T^∞, indicating that 16% of the total momentum was deposited between $z = H_\rho$ and z_r.

For the results in Figure 5(b) (corresponding to the simulations shown in Figures 3(d)–3(f) and 4(f)) the wavepacket reflection level is $z_r = 4H_\rho > z_\Delta$, in which case anelastic growth to weakly nonlinear amplitudes is significant before the wavepacket reaches the reflection level. As in Figure 5(a), when the wavepacket reaches the reflection level, a portion of the wavepacket extends across $z = z_r$. Here, however, the portion of the wavepacket that has crossed the reflection level irreversibly deposits its momentum to the background locally accelerating the background winds. At late times, $M_U^\infty = 0.05M_T$ is non-zero indicating permanent deposition of momentum above the reflection level. In the lower region, M_L^∞ only reaches 25% of its original value. The non-zero difference, $M_T^\infty - (M_L^\infty + M_U^\infty) = 0.61$, is the fraction of incident momentum irreversibly deposited to the background flow below the reflection level.

From the values of M_U^∞, M_L^∞, and M_T^∞ determined for a wide range of simulations, we compute the transmission and reflection coefficients using (32) and (33), respectively. These are plotted in Figure 6 along with values of $1 - (T + R)$, which is the relative amount of momentum lost to the background between H_ρ and z_r. In all cases where $z_r = H_\rho$, $T \simeq 0$ and $R \simeq 1$. In these low z_r/H_ρ cases,

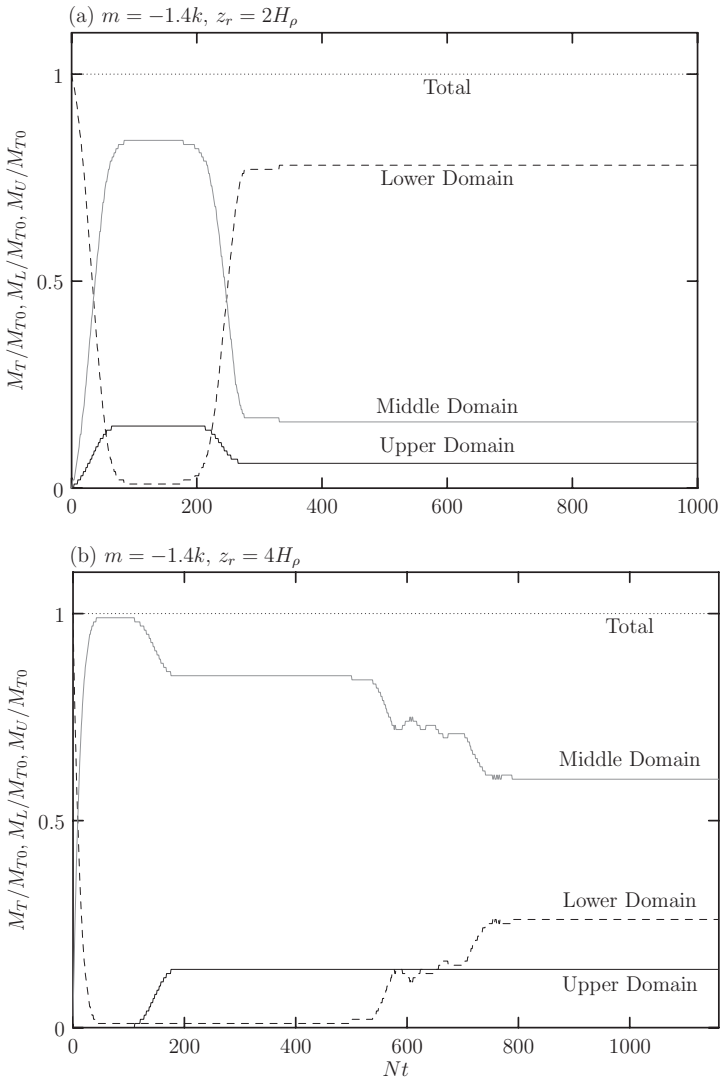

FIG. 5. Momentum in the whole domain – M_T (dotted), lower domain – M_L (dashed), middle domain – M_M (gray), and upper domain – M_U (solid) related to total momentum at $Nt = 0$, M_{T0}, shown as a function of time for simulations with $kH_\rho = 20$, $m = -1.4k$ and the reflection height at (a) $z_r = 2H_\rho$ and (b) $z_r = 4H_\rho$.

both z_Δ and z_b are significantly higher than the maximum amplitude reached by the wavepacket, as seen in Figures 2 and 4(a)–4(c).

Figure 6(a) shows that in weaker shear (so that waves propagate higher before encountering a reflection level and so become increasingly nonlinear due to anelastic growth), less momentum is returned to the lower domain at late times. Instead, the wavepacket either transmits above the reflection level or dissipates between $z = H_\rho$ and z_r. Whether significant transmission above z_r occurs (Figure 6(b)) or momentum is deposited moderately below z_r (Figure 6(c)) depends upon the initial vertical wavenumber, as indicated by the different symbols on each curve.

Of the four relative vertical wavenumbers examined, the steepest decrease in the reflection coefficient with increasing z_r/H_ρ occurs for the modulationally unstable case ($m = -0.4k$), with only a small amount of reflection occurring for $z_r \gtrsim 6H_\rho$. Up to 60% of the momentum is transmitted above the reflection level (for $z_r = 4H_\rho$), but as the shear weakens and z_r increases, the transmission coefficient decreases and most momentum is deposited below the reflection level for $z \gtrsim 6H_\rho$. Similar behavior is observed for the marginally stable case with $m = -0.7k$.

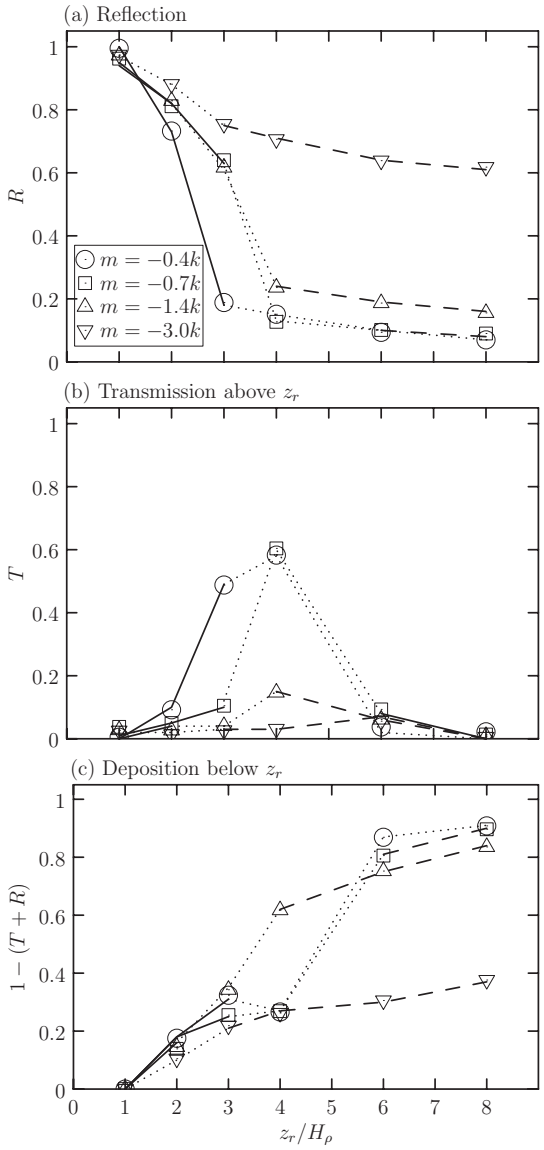

FIG. 6. Coefficients of (a) reflection and (b) transmission, and (c) the fraction of wave momentum deposited to the background flow for $H_\rho < z < z_r$. In all plots, $kH_\rho = 20$ ($\lambda_x/H_\rho = 0.3$) and $k\sigma = 10$. Solid lines are drawn between the points where $z_r < z_\Delta$, dotted lines are drawn between the points where $z_\Delta < z_r < z_b$, and dashed lines are drawn between the points where $z_r > z_b$. Different symbols are plotted for simulations with different values of m, as indicated in the legend in (a).

In the simulations with modulationally stable waves ($m = -1.4k$ and $-3k$), the reflection decreases less rapidly for $m = -1.4k$ and much less rapidly for $m = -3k$. Transmission remains small as z_r/H_ρ increases. The enhanced spreading and relative decrease in the wavepacket amplitude gives a result closer to that predicted by linear theory. The decrease in reflection coefficient with increasing z_r/H_ρ is accounted for by increasing deposition of momentum moderately below z_r. In part this occurs because the breaking level, z_b, predicted by linear theory in the absence of shear also occurs below z_r if $z_r/H_\rho \gtrsim 4H_\rho$. Dosser and Sutherland[16] showed that weakly nonlinear effects result in modulationally stable wavepackets breaking well above z_b. But this effect combined with wave reflections due to background shear results in momentum deposition and heights near z_r with more reflection and less momentum deposition occurring as $|m/k|$ increases.

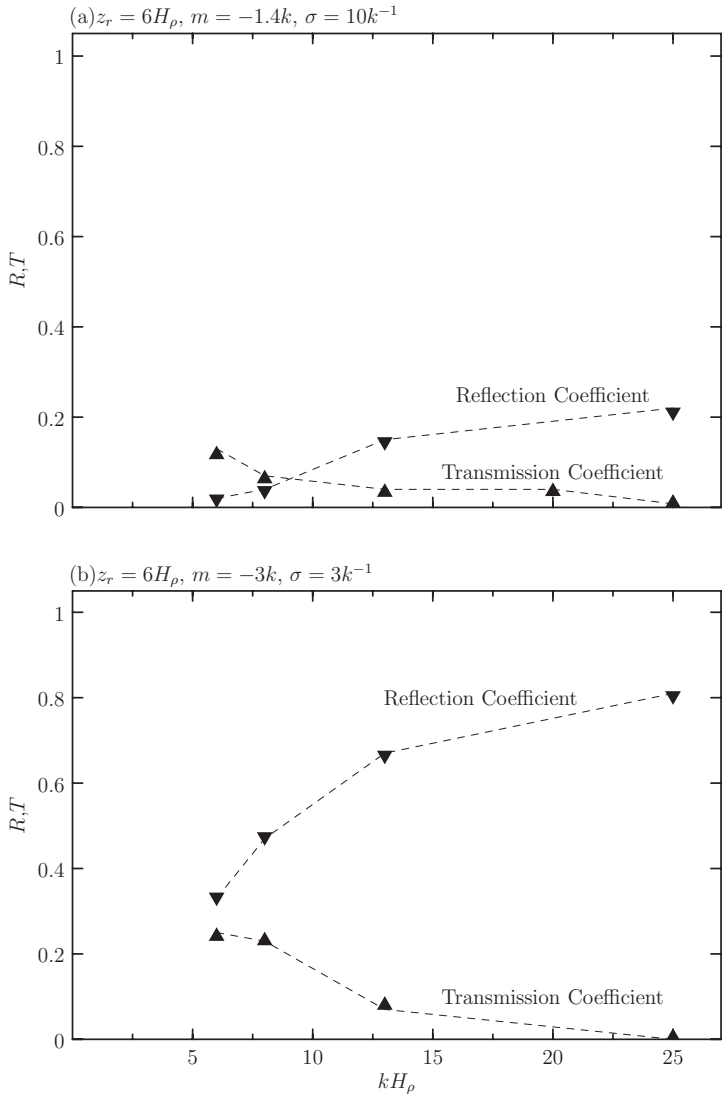

FIG. 7. Coefficients of reflection (downward triangles) and transmission (upward triangles) as a function of kH_ρ computed from simulations with (a) $m = -1.4k$, $\sigma = 10k^{-1}$ and (b) $m = -3.0k$, $\sigma = 3k^{-1}$. In all cases $z_r = 6H_\rho$. In (a) $z_\Delta \simeq 2.5H_\rho$ and $z_b \simeq 5.3H_\rho$. In (b) $z_\Delta \simeq 2.1H_\rho$ and $z_b \simeq 3.8H_\rho$.

Further simulations were also run to examine how the horizontal wavelength relative to density scale height affects transmission in the modulationally stable cases with $m = -1.4k$ and $m = -3k$. In the latter case we set the wavepacket width to be $\sigma = 3k^{-1}$, which still ensures that the wavepacket is quasi-monochromatic. kH_ρ ranged from 25 to 3 corresponding to the relative horizontal wavelength, λ_x/H_ρ, ranging from 0.3 to 2.

Figure 7 shows the computed reflection and transmission coefficients from simulations with the reflection height fixed at $z_r = 6H_\rho$. Figure 7(a) shows the reflection and transmission coefficients determined for simulations where $\sigma = 10k^{-1}$ and $m = -1.4k$ (as indicated by the upward triangles in Figure 6 for the specific case with $z_r = 6H_\rho$). As k decreases (λ_x increases) relative to H_ρ, greater reflection but less transmission is observed. For a narrower wavepacket with $\sigma = 3k^{-1}$ and $m = -3k$, similar behavior was observed. In these cases the reflection coefficient is smaller indicating that what does not transmit for the long wavelength cases deposits momentum near the reflection level.

VI. DISCUSSION AND CONCLUSIONS

The fully nonlinear anelastic equations were solved to examine the evolution of quasi-monochromatic internal wavepackets in background uniform retrograde shear. If the reflection level was situated at sufficiently low altitude that the wave amplitude remained small as it approached the level, the wavepacket entirely reflected as predicted by linear theory. However, if it was situated above the height, z_Δ, at which weakly nonlinear effects become important, then the wavepacket partially transmitted across the reflection level and some portion of the wavepacket permanently deposited momentum to the background flow below the reflection level. If z_r was well above z_Δ, all momentum for nonhydrostatic waves with $|m| \lesssim 0.7k$ was deposited below z_r even though $z_r < z_b$. When waves are modulationally unstable, the wave-induced mean flow becomes so large that it effectively shields the wavepacket from the effect of the background flow which, in turn, allows a significant portion of the wavepacket to transmit through the reflection level and continue upward propagation until anelastic growth becomes so large that the wave overturns. Conversely, when waves are stable, the wavepacket either reflects linearly (when $z_r < z_\Delta$) or deposits a significant portion of momentum to the background flow just below the reflection level (when $z_\Delta < z_r < z_b$) due to wave superposition. The wave-induced mean flow, its influence upon the modulational stability of the wavepacket, and its transient modification of the background wind determined the transmission, reflection, and relative momentum deposition coefficients.

Transmission was enhanced for modulationally unstable and marginally stable wavepackets whose amplitude envelope narrowed and grew sufficiently to counteract the Doppler-shifting influence of the background wind. Waves that transmitted continue to be Doppler-shifted and deposited their momentum over a vertical range above z_r. If z_r was very large, though still smaller than z_b, anelastic growth was so significant that waves dissipated before reaching the reflection level.

While Dosser and Sutherland[16] showed that modulationally stable waves (with large $|m/k|$) broke well above the breaking level predicted by linear theory, this study of waves in retrograde shear showed enhanced reflection and deposition below z_b even if $z_b > z_r$. This was due to transient amplitude growth as the leading, downward-propagating flank of the wavepacket superimposed upon the trailing, upward-propagating flank.

In order to make a more direct comparison between our numerical results and (more significantly energy-containing) atmospheric internal waves, we examined the impact of momentum transmission, reflection and deposition upon increasing relative horizontal wavelength expressed through decreasing kH_ρ. For $kH_\rho \lesssim 6$, corresponding to horizontal wavelengths $\lambda_x \gtrsim 8$ km, reflection was negligible with up to 20% of the momentum transmitting across the reflection level and the remainder being deposited moderately below the reflection level.

At mid-latitudes in the northern hemisphere winter[24] the typical shear and stratification in the stratosphere is $|s_0| \simeq 0.0018\,\mathrm{s}^{-1}$ and $N \sim 0.01\,\mathrm{s}^{-1}$. Taking $H_\rho = 8.4$ km and considering a wavepacket with initial vertical displacement amplitude approximately 1% of the horizontal wavelength, corresponding approximations can be made for R and T, and for the altitude, z_d, at which peak acceleration of the background flow occurs due to momentum deposition from either wave superposition or large-scale anelastic growth. These results are given in Table II.

For example, first consider an internal wave with $m = -3k$ ($\omega \simeq 0.003\ \mathrm{s}^{-1}$) at the tropopause. If the horizontal wavelength is $\lambda_x = 25$ km, the predicted reflection height is 15 km above. Our simulations show that all of the momentum will be reflected back toward the troposphere. Analogous to the simulations shown in Figs. 2 and 6, the wavepacket in this scenario has not undergone sufficient anelastic growth for nonlinear effects to become significant. Hence it is reasonable to predict that no portion of the wavepacket will transmit above the reflection level.

Next, consider a wavepacket with $m = -1.4k$ and $\lambda_x = 84$ km. Here, z_r lies above z_Δ but below z_b—similar to the simulation shown in Figs. 3(d)–3(f). Anelastic amplitude growth has become significant and nonlinear effects are expected to take hold. As seen in Figs. 3(d)–3(f), 6, and 7, little transmission or reflection is expected—in this case, only 14% transmission and 20% reflection. Major momentum deposition is expected to take place just below z_r due to superpositioning of the wavepacket as it undergoes reflection. This can be clearly seen in a similar simulation in Fig. 3(f). Hence, it would be expected that 66% of the wave momentum will be deposited 34 km

TABLE II. Predicted reflection height (z_r), predicted breaking height (z_b), predicted height at which nonlinear effects are expected to become significant (z_Δ), estimated height of maximum irreversible mean flow acceleration due to overturning (z_d), estimated reflection coefficient (R), and transmission coefficient (T), given for a range of λ_x and for $m = -1.4k$ and $m = -3k$. Values of R and T are estimated by scaling the results plotted in Figures 6 and 7 to match typical stratospheric conditions in northern hemisphere winter, for which $s_0 = 0.0018$ s^{-1} and $N = 0.01$ s^{-1}. In all cases the vertical extent of the wavepacket is $\sigma = 3k^{-1}$ and the wave amplitude at the bottom of the stratosphere (taken to be $z = 0$) is $A = 0.05k^{-1} \simeq 1\%\,\lambda_x$. No value of z_d is given if no overturning and hence no irreversible mean flow acceleration occurs.

	$m = -1.4k$						$m = -3k$					
λ_x (km)	z_r (km)	z_b (km)	z_Δ (km)	z_d (km)	R	T	z_r (km)	z_b (km)	z_Δ (km)	z_d (km)	R	T
25	9	45	31		1.0	0.0	15	32	17		1.0	0.0
42	16	45	31	16	0.90	0.01	25	32	17	25	0.78	0.01
59	23	45	30	23	0.61	0.05	36	32	17	32	0.23	0.10
84	35	44	28	34	0.20	0.14	51	32	16	32	0.05	0.03
101	44	44	26	44	0.17	0.05	62	32	16	32	0.0	0.01
118	53	44	26	44	0.05	0.0	73	32	15	32	0.0	0.0

above the tropopause, 20% will be reflected back toward the tropopause, and 14% will continue upward propagation toward the stratopause.

Finally, consider a wavepacket with $m = 3k$ and $\lambda_x = 101$ km. In this scenario, $z_b < z_r$ indicating that the wavepacket will become unstable well below the expected reflection height of 62 km. Similar to simulations presented in Fig. 6 where $z_r = 8H_\rho$, it is expected that the wavepacket will become unstable below z_r and momentum deposition will take place near z_b. In this case, it would be expected that the wavepacket will deposit its momentum roughly 32 km above the tropopause with only a small amount (1%) continuing to propagate upward.

While the reflection of internal waves can well be represented by 2D simulations, wave breaking is an inherently three-dimensional phenomenon. However, 2D simulations have been shown to well-capture the wave dynamics even during the early stages of wave breaking.[25] The results do not attempt to interpret, in detail, the dynamics of wave breaking but rather wave dynamics prior to breaking and consequent momentum deposition.

The buoyancy frequency and shear was uniform for all simulations. However, in the atmosphere, these change dramatically over very large amplitudes. Further research will use a fully nonlinear numerical code to analyze wavepacket interactions in non-uniform background shear and with non-uniform stratification. This research aims ultimately to provide more physically justifiable wave drag parameterization schemes through measurements of momentum deposition heights and strengths determined from fully resolved simulations of propagation and breaking.

APPENDIX: DERIVATION OF SCALED ANELASTIC EQUATIONS

Here we derive the formulae for the basic state fields solved by the numerical model. From the anelastic approximation to the continuity equation, $\nabla \cdot (\bar{\rho} u) = 0$, it follows that one can write the velocity components in terms of a mass streamfunction, ψ, according to

$$u = -\frac{1}{\bar{\rho}} \frac{\partial \psi}{\partial z} \tag{A1}$$

and

$$w = \frac{1}{\bar{\rho}} \frac{\partial \psi}{\partial x}. \tag{A2}$$

The spanwise vorticity is

$$\zeta = \frac{\partial u}{\partial z} - \frac{\partial w}{\partial x} = -\frac{1}{\bar{\rho}} \left[\nabla^2 \psi + \frac{1}{H_\rho} \frac{\partial \psi}{\partial z} \right], \tag{A3}$$

in which $H_\rho = -\left(\frac{\bar{\rho}'}{\bar{\rho}}\right)^{-1}$ is the density scale height.

Neglecting viscosity, the fully nonlinear momentum equations for an anelastic gas are

$$\frac{Du}{Dt} = -\frac{\partial}{\partial x}\left(\frac{p}{\bar{\rho}}\right) \tag{A4}$$

and

$$\frac{Dw}{Dt} = -\frac{\partial}{\partial z}\left(\frac{p}{\bar{\rho}}\right) + \frac{g}{\bar{\theta}}\theta. \tag{A5}$$

Taking the curl of the momentum conservation equations, the equation for evolution of vorticity is

$$\frac{D\zeta}{Dt} = -\frac{1}{H_\rho} w\zeta - \frac{g}{\bar{\theta}}\frac{\partial \theta}{\partial x}. \tag{A6}$$

Neglecting thermal diffusion, the internal energy equation is

$$\frac{D\theta}{Dt} = -w\frac{d\bar{\theta}}{dz}. \tag{A7}$$

Rather than work with θ, we cast the internal energy equation more intuitively in terms of ξ, defined implicitly by

$$\theta = -\frac{d\bar{\theta}}{dz}\xi. \tag{A8}$$

The quantity ξ well approximates the vertical displacement field if the displacement is much smaller compared with the potential temperature scale height, H_θ. Likewise, we approximate $d\bar{\theta}/dz$ as locally constant upon substituting (A8) into (A7) to give

$$\frac{D\xi}{Dt} = w. \tag{A9}$$

Due to the exponential decrease of $\bar{\rho}$, the basic state fields are expected to change exponentially at leading order in linear theory. Accounting for this, we work with variables that do not exhibit such exponential changes. These "hatted" variables are defined implicitly by

$$\begin{aligned}
\zeta(x,z,t) &= \hat{\zeta}(x,z,t)e^{z/2H_\rho},\\
\vec{u}(x,z,t) &= \hat{\vec{u}}(x,z,t)e^{z/2H_\rho},\\
\theta(x,z,t) &= \hat{\theta}(x,z,t)e^{z/2H_\rho}e^{z/H_\theta},\\
\psi(x,z,t) &= \hat{\psi}(x,z,t)e^{-z/2H_\rho},\\
\xi(x,z,t) &= \hat{\xi}e^{z/2H_\rho}.
\end{aligned} \tag{A10}$$

Relationships for the above variables to the streamfunction can be found in Table I.

By applying the scalings in (A10) to (A6) and (A9), the evolution equations for $\hat{\zeta}$ and $\hat{\xi}$ are

$$\frac{\partial \hat{\zeta}}{\partial t} = e^{z/2H_\rho}\left[-\hat{u}\hat{\zeta}_x - \hat{w}\hat{\zeta}_z - \frac{3}{2H_\rho}\hat{w}\hat{\zeta}\right] + N^2\hat{\xi}_x \tag{A11}$$

and

$$\frac{\partial \hat{\xi}}{\partial t} = e^{z/2H_\rho}\left[-\hat{u}\hat{\xi}_x - \hat{w}\hat{\xi}_z - \left(\frac{1}{2H_\rho} + \frac{1}{H_\theta}\right)\hat{w}\hat{\xi}\right] + \hat{w}. \tag{A12}$$

The final step is to include the background flow, $\bar{U}$, in (A11) and (A12) giving

$$\frac{\partial}{\partial t}\hat{\zeta} = -\bar{U}\hat{\zeta}_x + e^{z/2H_\rho}\left[-\hat{u}\hat{\zeta}_x - \hat{w}\hat{\zeta}_z - \frac{3}{2H_\rho}\hat{w}\hat{\zeta}\right] + N^2\hat{\xi}_x \tag{A13}$$

and

$$\frac{\partial}{\partial t}\hat{\xi} = -\bar{U}\hat{\xi}_x + e^{z/2H_\rho}\left[-\hat{u}\hat{\xi}_x - \hat{w}\hat{\xi}_z - \left(\frac{1}{2H_\rho} + \frac{1}{H_\theta}\right)\hat{w}\hat{\xi}\right] + \hat{w}. \tag{A14}$$

Including diffusion in (A13) and (A14) gives (22) and (23), which are explicitly solved by the numerical code.

[1] F. P. Bretherton, "Momentum transport by gravity waves," Q. J. R. Meteorol. Soc. **95**, 213–243 (1969).
[2] C. McLandress, "On the importance of gravity waves in the middle atmosphere and their parameterization in general circulation models," J. Atmos. Sol.-Terr. Phys. **60**, 1357–1383 (1998).
[3] T. N. Palmer, G. J. Shutts, and R. Swinbank, "Alleviation of a systematic westerly bias in general circulation and numerical weather prediction models through an orographic gravity drag parametrization," Q. J. R. Meteorol. Soc. **112**, 1001–1039 (1986).
[4] N. A. McFarlane, "The effect of orographically excited gravity wave drag on the general circulation of the lower stratosphere and troposphere," J. Atmos. Sci. **44**, 1775–1800 (1987).
[5] K. Hamilton, "Comprehensive meteorological modelling of the middle atmosphere: A tutorial review," J. Atmos. Terr. Phys. **58**, 1591–1627 (1996).
[6] R. S. Lindzen, "Turbulence and stress owing to gravity wave and tidal breakdown," J. Geophys. Res. **86**, 9707–9714, doi:10.1029/JC086iC10p09707 (1981).
[7] G. D. Nastrom and D. C. Fritts, "Sources of mesoscale variability of gravity waves. Part I: Topographic excitation," J. Atmos. Sci. **49**, 101–110 (1992).
[8] A. S. Medvedev and G. P. Klaassen, "Vertical evolution of gravity wave spectra and the parameterization of associated wave drag," J. Geophys. Res. **100**, 25841–25853, doi:10.1029/95JD02533 (1995).
[9] C. O. Hines, "Doppler-spread parameterization of gravity-wave momentum deposition in the middle atmosphere. Part 1: Basic formulation," J. Atmos. Sol.-Terr. Phys. **59**, 371–386 (1997).
[10] C. Staquet and J. Sommeria, "Internal gravity waves: From instabilities to turbulence," Annu. Rev. Fluid Mech. **34**, 559–593 (2002).
[11] T. J. Dunkerton, "Wave transience in a compressible atmosphere. Part I: Transient internal wave, mean-flow interaction," J. Atmos. Sci. **38**, 281–297 (1981).
[12] B. R. Sutherland, "Weakly nonlinear internal wavepackets," J. Fluid Mech. **569**, 249–258 (2006).
[13] D. C. Fritts and T. J. Dunkerton, "A quasi-linear study of gravity-wave saturation and self-acceleration," J. Atmos. Sci. **41**, 3272–3289 (1984).
[14] B. R. Sutherland, "Finite-amplitude internal wavepacket dispersion and breaking," J. Fluid Mech. **429**, 343–380 (2001).
[15] H. V. Dosser and B. R. Sutherland, "Weakly nonlinear non-Boussinesq internal gravity wavepackets," Physica D **240**, 346–356 (2011).
[16] H. V. Dosser and B. R. Sutherland, "Anelastic internal wavepacket evolution and stability," J. Atmos. Sci. **68**, 2844–2859 (2011).
[17] B. R. Sutherland, "Internal wave reflection in uniform shear," Q. J. R. Meteorol. Soc. **126**, 3255–3287 (2000).
[18] B. R. Sutherland and P. F. Linden, "An experimental/numerical study of internal wave transmission across an evanescent level," in *Mixing and Dispersion in Stably Stratified Flows*, edited by P. A. Davies (Oxford University Press, IMA, 1999), pp. 251–262.
[19] B. R. Sutherland, *Internal Gravity Waves* (Cambridge University Press, Cambridge, UK, 2010), p. 378.
[20] M. E. McIntyre, "On the wave momentum myth," J. Fluid Mech. **106**, 331–347 (1981).
[21] J. F. Scinocca and T. G. Shepherd, "Nonlinear wave-activity conservation laws and Hamiltonian structure for the two-dimensional anelastic equations," J. Atmos. Sci. **49**, 5–27 (1992).
[22] G. B. Whitham, *Linear and Nonlinear Waves* (John Wiley and Sons, Inc., New York, USA, 1974), p. 636.
[23] B. R. Sutherland and W. R. Peltier, "Turbulence transition and internal wave generation in density stratified jets," Phys. Fluids **6**, 1267–1284 (1994).
[24] E. Fleming, S. Chandra, M. Shoeberl, and J. Barnett, "Monthly mean global climatology of temperature, wind, geopotential height, and pressure for 0–120 km," Technical Report No. 100697, NASA, 1988.
[25] T. Lund and D. C. Fritts, "Numerical simulation of gravity wave breaking in the lower thermosphere," J. Geophys. Res. **117**, D21105, doi:10.1029/2012JD017536 (2012).